Attitude estimation for unresolved agile space objects with shape model uncertainty*

Marcus J. Holzinger†‡, Kyle T. Alfriend†, Charles J. Wetterer§, K. Kim Luu¶, Chris Sabol‡, Kris Hamada†, and Andrew Harms‖

Abstract

The problem of estimating attitude for actively maneuvering or passively rotating Space Objects (SOs) with unknown mass properties / external torques and uncertain shape models is addressed. To account for agile SO maneuvers, angular rates are simply assumed to be random inputs (e.g., process noise), and model uncertainty is accounted for in a bias state with dynamics derived using first principles. Bayesian estimation approaches are used to estimate the resulting severely non-Gaussian and multi-modal state distributions. Simulated results are given, conclusions regarding performance are made, and future work is outlined.

1 INTRODUCTION

The increasing number of manufactured on-orbit objects as well as improving sensor capabilities indicate that the number of trackable objects will likely exceed 100,000 within the next several years [1]. Characterizing these objects as completely as possible supports key objectives such as ensuring space operations and spaceflight safety, implementing international treaties and agreements, protecting space capabilities, and preserving national interests [2].

Characterizing the large population of non-spatially resolved active spacecraft, retired spacecraft, rocket bodies, debris, and High Area to Mass Ratio (HAMR) objects necessarily involves both attitude and shape estimation. While spatially unresolved Space Objects (SOs) cannot be directly imaged, attitude and shape may be inferred by carefully examining their lightcurves. Lightcurves are temporally-resolved sequences of photometric intensity measurements over one or more bandwidths. Because the observable reflected light from an unresolved SO is a strong function of both its shape and attitude, estimating these parameters using lightcurves can provide an avenue to determine both SO attitude and shape. This problem is traditionally called 'lighcurve inversion.'

While lightcurves have been used for at least 25 years to characterize spin states and shapes of asteroids (for an introduction see [3, 4]), estimating the attitude states and shapes of manufactured SOs involves a new set of challenges. New challenges addressed in this paper are 1) An active (agile) SO is often directly controlling its attitude, meaning that torques acting on the SO are not necessarily zero (non-homogeneous motion) and mass properties may not be known, motivating different dynamics assumptions. 2) Manufactured SOs may be quite symmetric about at least one axis of rotation/reflection, leading to multiple possible attitude estimate solutions and suggesting the use of non-Gaussian estimation approaches. 3) Shape models must often be estimated, and analytical / experimental reflectance models are at best approximations. As such, these shape models contain errors that need to be accounted for in the measurement function and state space using carefully derived bias dynamics. Using estimated shape models without accounting for the discrepancy with truth can often result in filter divergence, particularly under glint conditions. Combined,

*This work is sponsored by the Air Force Research Laboratory at the Air Force Maui Optical and Supercomputing site (AMOS).

†School of Aerospace Engineering, Georgia Institute of Technology

‡Aerospace Engineering Department, Texas A&M University

§Pacific Defense Solutions, LLC

¶Air Force Research Laboratory, USAF

‖Department of Electrical Engineering, Princeton University

these challenges make SO attitude estimation using lightcurves a difficult endeavor that is unique from the analogous asteroid problem, and provide the motivation for the approaches and contributions in this paper.

Hall et al. were the first to discuss lightcurve inversion as applied to SO attitude and shape determination with many observations and results paralleling developed theory in the asteroid literature [5]. Approaches to decouple the simultaneous SO attitude/shape estimation problem into separate attitude and shape estimation problems have also been proposed [6]. For shape-independent attitude estimation, both differences in synodic and sidereal periodicities and isolating facet orientations using glints have been investigated. Attitude-independent shape estimation is approached using the solar phase angle to decouple attitude and shape. Importantly, identifying differences in synodic and sidereal periodicities using a Fourier series decomposition helped determine the spin-rate and axis of NASA's IMAGE satellite after an on-board spacecraft anomaly in 2005 [7].

Simulated lightcurve data using the Cook-Torrance [8] Bidirectional Reflectivity Distribution Function (BRDF) model was first applied in a batch estimation framework to ellipsoidal SO models in geostationary orbits [9]. The Ashikhmin-Shirley [10] BRDF has also been used to study estimation of specular reflectivity, diffuse reflectivity, emissivity, and projected facet area [11]. The first use of lighcurves to sequentially estimate SO attitude assumed a non-convex 300 facet model and simulated lightcurves using a combination of Lambertian and Cook-Torrance (specular) BRDF models with an Unscented Kalman Filter (UKF) [12]. Linares et al. have used Multiple Model Adaptive Estimation (MMAE) to circumvent shape ambiguity issues while concurrently estimating SO attitude using sequential estimation [13]. In this work, multiple candidate models were concurrently assumed in individual sequential UKFs and fit metrics were used to compute probabilities that a particular model best matches lightcurve observations.

Thus far, sequential lightcurve attitude estimation has typically used UKFs to circumvent the nonlinearity inherent in the system dynamics and uncertainty propagation, as well as to avoid computing excessively complicated partial derivatives. With UKFs, however, a potential shortcoming is evident. Using a specular BRDF model such as Cook-Torrance, the measurement function is exceedingly nonlinear. Because of this nonlinearity, and the potential existence of multiple solutions, the true a posteriori probability distribution functions (PDFs) may be quite non-Gaussian and potentially multi-modal, for which a UKF is not particularly suited.

This effort explores the use of Bayesian sequential estimation to address several of the challenges in SO attitude estimation from lightcurves. The primary benefits of using a Bayesian filter for a lightcurve-based attitude estimator are that 1) no linearizations about nominal trajectories or expected measurements are used, and 2) arbitrary PDFs may be point-wise approximated [14]. Because no linearizations are made and arbitrary PDFs may be approximated, initial PDFs may be taken as uniform distributions spanning large regions of the parameter space and multiple potential solutions for symmetric spacecraft may be identified. This is particularly useful for attitude estimation, as attitude parameters are often bounded over specific regions, allowing an initial uniform distribution to encompass all possible SO attitudes.

This paper is a summary of a companion journal paper [15]. The contributions of this effort are a) the inclusion of mean angular rate and angular rate uncertainty to account for agile SO dynamics, b) the derivation of shape model measurement bias dynamics based on a first principles approach to accounting for shape model uncertainty, c) the use of a Particle Filter to successfully track actively maneuvering SOs, and d) the use of a Particle Filter to estimate SO attitude in the presence of shape model uncertainty.

The remainder of this paper is organized as follows. The system dynamics, agile SO dynamics, measurement equations, shape model bias dynamics, and fundamentals of Bayesian estimation are introduced. Next, specific PF algorithms are introduced and discussed, the simulation is described in detail, and the results for five separate test cases are presented. Lastly a summary is made and future work is suggested.

2 DYNAMICS AND MEASUREMENT MODELS

In this section, attitude dynamics are briefly discussed, followed by a detailed definition and discussion of the lightcurve measurement model and shape model bias dynamics derivation. The section concludes by combining the attitude and bias dynamics, introducing principles behind Bayesian estimation, and outlining the specific implementation of the particle filter used in this paper.

2.1 Dynamics

The rotation from the Inertial frame $\mathcal{I}$ to the SO body frame $\mathcal{B}$ is defined using the attitude coordinate $\boldsymbol{\theta}_{\mathcal{I}}^{\mathcal{B}}$. The dynamics of $\boldsymbol{\theta}_{\mathcal{I}}^{\mathcal{B}}$ and the angular velocity $\boldsymbol{\omega}$ are [16]

$$\begin{bmatrix} \dot{\boldsymbol{\theta}}_{\mathcal{I}}^{\mathcal{B}} \\ \mathbf{J}\dot{\boldsymbol{\omega}} \end{bmatrix} = \begin{bmatrix} \mathbf{B}\left(\boldsymbol{\theta}_{\mathcal{I}}^{\mathcal{B}}\right)\boldsymbol{\omega} \\ -\boldsymbol{\omega}\times\mathbf{J}\boldsymbol{\omega} + \boldsymbol{\tau} \end{bmatrix} \tag{1}$$

Here, $\mathbf{B}(\boldsymbol{\theta}_{\mathcal{I}}^{\mathcal{B}})$ is a kinematic mapping from the instantaneous angular rate vector to the instantaneous attitude parameter time derivatives. For simplicity the body frame $\mathcal{B}$ of the SO is chosen such that $\mathbf{J}$ is diagonal with diagonal elements J_1, J_2, and J_3, where the principle axes of inertia satisfy the inequality $J_1 \geq J_2 \geq J_3 > 0$. As discussed in the introduction, the mass properties and torques acting on an SO are not necessarily known, so it is necessary to make some assumptions to propagate (1). Fortunately, there are practical limits to angular rates in operational spacecraft (e.g., sensors, actuation authority) that reduce the scope of this problem. In this paper, it is assumed that $\mathbf{J}$ and $\boldsymbol{\tau}$ are such that at any particular instant, the angular velocity $\boldsymbol{\omega}$ can be written as

$$\boldsymbol{\omega} = \boldsymbol{\omega}_{\mu} + \delta\boldsymbol{\omega} \tag{2}$$

where $\boldsymbol{\omega}_{\mu}$ satisfies the equality $\boldsymbol{\omega}_{\mu}\mathbf{J} = -\boldsymbol{\omega}_{\mu}\times\mathbf{J}\boldsymbol{\omega}_{\mu}$ and $\delta\boldsymbol{\omega} \sim N(\mathbf{0}, \mathbf{Q}_{\omega})$. It is assumed here that $\boldsymbol{\omega}_{\mu}$ is known, as with the majority of SOs (e.g., geostationary spacecraft, LEO spacecraft), mean rotation rates can be assumed based on SO function (once a day for geostationary, once per orbit for weather satellites, etc.). If $\boldsymbol{\omega}_{\mu}$ is unknown, it can be assumed to be zero and the angular rate uncertainty can be increased. The covariance matrix $\mathbf{Q}_{\omega}$ from which $\delta\boldsymbol{\omega}$ is drawn can be chosen such that $\delta\boldsymbol{\omega}$ is representative of maneuvering spacecraft capabilities (e.g., 0.1 deg/s, 0.5 deg/s). Using this approach, mean motion (like nadir pointing or sun pointing) is captured, and motion about these nominal dynamics may be modeled as process noise. The simplified dynamics using (2) are

$$\dot{\boldsymbol{\theta}}_{\mathcal{I}}^{\mathcal{B}} = \mathbf{B}\left(\boldsymbol{\theta}_{\mathcal{I}}^{\mathcal{B}}\right)\left(\boldsymbol{\omega}_{\mu} + \delta\boldsymbol{\omega}\right) \tag{3}$$

In addition to not requiring knowledge of SO mass properties or torques, an additional benefit of this model reduction approach is that the dimensionality has ben reduced to only the attitude states.

2.2 Measurement Model

The observed reflected light of a rigid body is a function of several parameters. Before a measurement and error model may be constructed, reflection geometry and the fundamental principles behind shape models and BRDFs bear discussion. Figure 1(a) describes the inertial geometry of the SO, Observer, and Sun, and figure 1(b) depicts the geometry of the light reflection problem for a point on the surface of a rigid body.

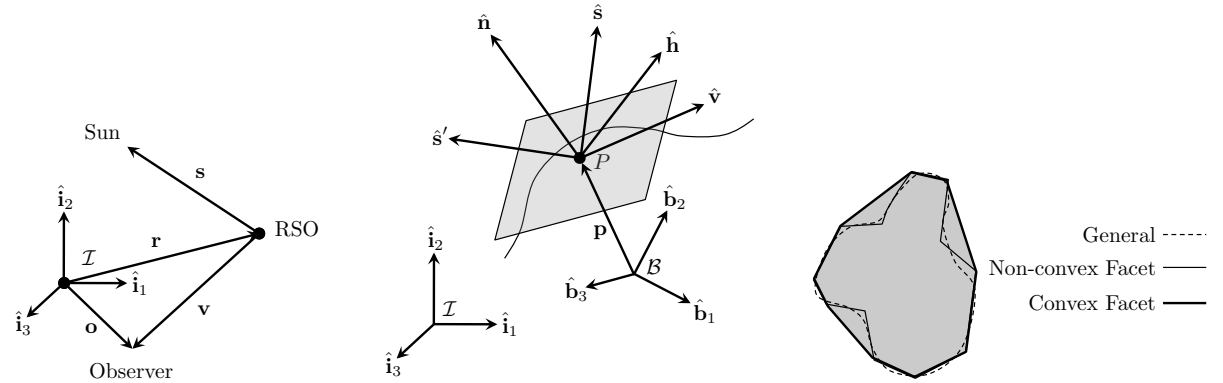

(a) Inertial geometry for the SO (**r**), Observer (**o**), and illumination source (Sun, **s**)

(b) Reflection geometry for a point on the surface of a rigid body

(c) Shape model illustration of a general, non-convex, and convex notional shape model

Figure 1: Inertial / local observation geometries and shape model visualization

The unit vector $\hat{\mathbf{s}}$ points toward the light source (the sun), $\hat{\mathbf{v}}$ points towards the observer, $\hat{\mathbf{n}}$ is the normal vector of the surface at point P (where P is located at $\mathbf{p}$), $\hat{\mathbf{h}}$ is the bisector between $\hat{\mathbf{s}}$ and $\hat{\mathbf{v}}$, $\mathcal{B}:\{\hat{\mathbf{b}}_1,\hat{\mathbf{b}}_2,\hat{\mathbf{b}}_3\}$ is the body frame, and $\mathcal{I}:\{\hat{\mathbf{i}}_1,\hat{\mathbf{i}}_2,\hat{\mathbf{i}}_3\}$ is the inertial frame.

As outlined in the Introduction, the majority of shape models used in the empirical asteroid lightcurve inversion literature are convex facet shape models [17, 18, 19]. Further, if the shape of an SO is reasonably well known (perhaps from mechanical drawings), a batch estimation process may conceivably estimate the surface material reflectance properties, yielding a potentially non-convex shape model. Largely following the notation of Hall et al. [5] and making body-frame coordinates explicit, for a general (convex or nonconvex) facet shape model, For facet shape models, the apparent magnitude of over wavelengths Λ is written as

$$M(\boldsymbol{\theta}^{\mathcal{B}}_{\mathcal{I}},\mathbf{s},\mathbf{v},\mathbf{p}) = -2.5\log_{10}\left\{\frac{1}{\mathbf{v}^T\mathbf{v}}\int_{\Lambda}\Im_s(\mathbf{s},\lambda)\left(\sum_{i=1}^{N_f}A_{i,vis}\rho_i({}^{\mathcal{B}}\hat{\mathbf{s}},{}^{\mathcal{B}}\hat{\mathbf{v}};{}^{\mathcal{B}}\hat{\mathbf{n}}_i,\mathbf{p}_i,\lambda)\right)\mathrm{d}\lambda\right\} - 26.74 \tag{4}$$

where $\Im_s(\mathbf{s},\lambda)$ is the illumination of the light source (here, the Sun), N_f is the number of facets, $A_{i,vis}$ is the projected visible area of facet i, $\rho_i({}^{\mathcal{B}}\hat{\mathbf{s}},{}^{\mathcal{B}}\hat{\mathbf{v}};{}^{\mathcal{B}}\hat{\mathbf{n}}_i,\mathbf{p}_i,\lambda)$ is the weighted BRDF model with one or more constituent BRDF models (e.g., Lambertian, Cook-Torrance, Ashikhmin-Shirley), ${}^{\mathcal{B}}\hat{\mathbf{n}}_i$ is the facet normal unit vector in the body frame, and $\mathbf{p}_i$ contains the BRDF parameters for facet i. A notional illustration of the differences between general-, nonconvex facet-, and convex facet-shape models is shown in Figure 1(c).

To construct an approximate measurement function in analytical form a BRDF function ρ_i must be chosen for (4). Based on these empirically derived performance rankings [20, 21], either He-Torrance or Cook-Torrance appear to be acceptable BRDF model candidates for SO specular lightcurve modeing efforts. It remains a focus of future work to improve the physics behavior of BRDF models in general. Often two or more reflectance models are affinely combined to account for both diffuse and specular reflectance. The Cook-Torrance BRDF model [8] is used here for specular modeling and Lambertian reflectance is used for diffuse modeling. The composite BRDF model is

$$\rho_i({}^{\mathcal{B}}\hat{\mathbf{s}},{}^{\mathcal{B}}\hat{\mathbf{v}};{}^{\mathcal{B}}\hat{\mathbf{n}}_i,\xi_i,a_i,n_i,m_i) = \xi_i R_d({}^{\mathcal{B}}\hat{\mathbf{n}}_i,{}^{\mathcal{B}}\hat{\mathbf{s}};a_i) + (1-\xi_i)R_s({}^{\mathcal{B}}\hat{\mathbf{s}},{}^{\mathcal{B}}\hat{\mathbf{v}};{}^{\mathcal{B}}\hat{\mathbf{n}}_i,n_i,m_i) \tag{5}$$

where $\xi_i \in [0,1]$ is the convex mixing fraction parameter. In (5), for the i^{th} facet $a_i \in [0,1]$ is the diffuse albedo, n_i is the index of refraction, and m_i is the micro-facet slope parameter. In its final form, for each distinct frequency bandpass Λ_j, the measurement function is expressed in apparent magnitude as

$$\mathbf{z}_k = \mathbf{h}_k(\mathbf{x}_k,k) + \mathbf{w}_k = M_{\Lambda,j}(\boldsymbol{\theta}^{\mathcal{B}}_{\mathcal{I}}(t_k);\mathbf{s}(t_k),\mathbf{v}(t_k),\mathbf{p}) + b_j(t_k) + w_{j,k} \tag{6}$$

The measurement $\mathbf{z}_k \in \mathbb{R}^m$ and the facet model parameters, $\hat{\mathbf{n}}_i$ and $\mathbf{p}_i$ are assumed to be known (or estimated), b_j is the sensor bias, and $w_{j,k}$ is the instantiations of arbitrary measurement noise distribution. Past work has suggested that for the AEOS 3.6m telescope, band-averaged I-band measurement uncertainties are on the order of 0.3 mag, 3-σ [22]. Calibration, shape model, and BRDF errors are considered in the next subsection.

2.3 Measurement Bias Dynamics Derivation

This section summarizes the results derived in [15]. Supposing that photometric observations are used to measure apparent magnitudes over wavelengths Λ_j, the intensity measurement noise $\mathbf{w}_k$ may be considered a Gaussian white noise with $\mathbf{w}_k \sim N(\mathbf{0},\mathbf{R}_k)$. Further, it is often the case that a photometric observations have un-calibrated, potentially time-varying biases b_j in measured apparent intensity. Additionally, the effect of shape model uncertainty must be properly captured in the measurement function. When a shape model is built, there are typically fixed (non-time varying) modeling errors. Even with manufacturing level shape detail (such as can be obtained from CAD models), modeling errors in surface properties, the extended effects of space weathering, and other effects (such as wrinkles in mylar surfaces) are rarely captured exactly. Coupled with the fact that the timing and magnitude of glints contains significant information regarding spacecraft attitude $\boldsymbol{\theta}^{\mathcal{B}}_{\mathcal{I}}$, it is critical that the uncertainty in modeling parameters be quantified and accounted for. If the model uncertainty is not considered, discrepancies between the observed intensity and the modeled

intensity can cause filters to diverge. For each measurement frequency and bandpass, an ideal apparent magnitude measurement z_i (without CCD bias or noise) may be computed using

$$z_j = M_{\Lambda,j}(\boldsymbol{\theta}_{\mathcal{I}}^{\mathcal{B}}; \mathbf{s}, \mathbf{v}, \mathbf{p}) \tag{7}$$

After significant manipulation (given in detail in [15]) it can be shown that the addition of a bias state $b_{m,j}$ allows systemic uncertainty in the SO shape model to be accounted for. The dynamics of the bias state can be written as

$$\dot{b}_{m,j} = \eta_{\dot{b}_{m,j}} \tag{8}$$

with $\eta_{\dot{b}_{m,j}} \sim N(0, Q_{\dot{b}_{m,j}})$, where

$$Q_{\dot{b}_{m,j}} = \sum_{i=1}^{N_f} \left\{ \left(\boldsymbol{\omega}_\mu^T \mathbf{F}_i + (\dot{\mathbf{o}} - \dot{\mathbf{r}})^T \mathbf{G}_i^T\right) \mathbf{Q}_{p,i} \left(\mathbf{G}_i(\dot{\mathbf{o}} - \dot{\mathbf{r}}) + \mathbf{F}_i \boldsymbol{\omega}_\mu\right) + \mathrm{Tr}\left[\mathbf{F}_i^T \mathbf{Q}_{p,i} \mathbf{F}_i \mathbf{Q}_\omega\right] \right\} \tag{9}$$

with

$$\mathbf{F}_i = \left.\frac{\partial M_{\Lambda,j}}{\partial \mathbf{p}_i \partial \boldsymbol{\theta}_{\mathcal{I}}^{\mathcal{B}}}\right|_i \mathbf{B}(\boldsymbol{\theta}_{\mathcal{I}}^{\mathcal{B}}) \text{ and } \mathbf{G}_i = \left.\frac{\partial M_{\Lambda,j}}{\partial \mathbf{p}_i \partial \mathbf{v}}\right|_i$$

Eq. (9) has two terms; the first incorporates the relative velocity of the object $(\dot{\mathbf{o}} - \dot{\mathbf{r}})$ as well as the known angular motion $\boldsymbol{\omega}_\mu$ with the facet parameter uncertainty described by $\mathbf{Q}_{p,i}$. Note that as the relative velocity $(\dot{\mathbf{o}} - \dot{\mathbf{r}})$ or the nominal angular rate $\boldsymbol{\omega}_\mu$ increase, the uncertainty in the shape model bias dynamics strictly increases. The second term accounts for cross-coupling between angular rate uncertainty and facet parameter uncertainty, and becomes appreciable when $\mathbf{Q}_{p,i}$ and $\mathbf{Q}_\omega$ are large. Critically, the shape mode bias dynamics uncertainty strictly increases with both $\mathbf{Q}_{p,i}$ and $\mathbf{Q}_\omega$. These observations provide important performance guidelines. With an uncertain shape model, when the object has high nominal angular rates or is moving fast relative to the observer, bias uncertainty increases and attitude estimation performance should decrease. Naturally this is also the case when shape model facet uncertainty $\mathbf{Q}_{p,i}$ or maneuver angular rates represented by $\mathbf{Q}_\omega$ are large. In the following subsection the bias dynamics above in Eq. (9) will be combined with the rigid body dynamics.

2.4 Combined Bias and Rigid Body Dynamics

A straightforward combination of the simplified attitude dynamics (3) and shape model error bias dynamics (8) provides the final form of the dynamics used in this effort. Taken together, the combined dynamics are

$$\begin{bmatrix} \dot{\boldsymbol{\theta}}_{\mathcal{I}}^{\mathcal{B}} \\ \dot{b}_m \end{bmatrix} = \begin{bmatrix} \mathbf{B}(\boldsymbol{\theta}_{\mathcal{I}}^{\mathcal{B}})\boldsymbol{\omega}_\mu \\ 0 \end{bmatrix} + \begin{bmatrix} \mathbf{B}(\boldsymbol{\theta}_{\mathcal{I}}^{\mathcal{B}}) & \mathbf{0} \\ \mathbf{0} & 1 \end{bmatrix} \begin{bmatrix} \delta\boldsymbol{\omega} \\ \eta_{\dot{b}_m} \end{bmatrix} \tag{10}$$

The above equation assumes a single measurement channel ($j = 1$), though of course if multiple channels exist then multiple shape model bias terms may be used. The discrete-time dynamics used in the Particle Filter are generated using (10) and have the form

$$\mathbf{x}_k = \mathbf{f}_{k-1}(\mathbf{x}_{k-1}; \boldsymbol{\omega}_\mu) + \mathbf{v}_{k-1} \tag{11}$$

where $\mathbf{x}^T = \begin{bmatrix} (\boldsymbol{\theta}_{\mathcal{I}}^{\mathcal{B}})^T & b_m \end{bmatrix}$ and $\mathbf{v}_{k-1} \sim N(\mathbf{0}, \mathbf{Q}_{v,k-1})$.

2.5 Particle Filter Implementation

The Sample Importance Resampling (SIR) Particle Filter (also known as the Bootstrap Filter) and Systematic Resampling algorithms described by Ristic et al. [14] are shown are used to generate results in this paper. Further detail on the SIR Particle Filter and the Systematic Resampling algorithms may be found in [23] and [24], respectively. The SIR Particle Filter is ideal for the application at hand as both the dynamics (10) and measurement equation (6) are nonlinear, and there exists sufficient process noise in the system to avoid sample impoverishment issues.

3 SIMULATION RESULTS & DISCUSSION

The impact of incorporating the reduced order attitude dynamics and shape model bias dynamics in the filter are illustrated here using simulation. Five test cases (TCs) are investigated and summarized in Table 1. A baseline TC is given to demonstrate nominal PF performance when the true shape model is known and the SO is not maneuvering. The purpose of TC 1 is to demonstrate PF behavior in the presence of uncompensated shape model error while the SO maintains a stationary inertial attitude (dynamics are 'none'). This TC 1 is expected to diverge, however it provides an excellent comparison point for the baseline TC and TC 2, which incorporates the shape model bias state and dynamics defined in (8) (dynamics are 'bias'). TC 3 includes the uncertainty terms in angular velocity and demonstrates successful tracking of a maneuvering SO (dynamics are 'ang. rate'). TC 4 illustrates how a maneuvering SO with a shape model incorporating significant uncertainty may (crudely) have its attitude estimated (dynamics are 'ang. rate & bias'). All test cases use the GEOSAT spacecraft orbit and have a start time of December 17, 2009, 4:47:15 UT. Observations are simulated from the Advanced Electro-Optical System (AEOS) telescope in Maui, HI for 350 seconds with a 5 second measurement frequency (71 measurements) and 0.3 mag (1-σ) apparent magnitude noise. The example scenarios use 3-2-1 Euler angle parameters to describe the attitude state. The baseline TC, TC 1, and TC 2 incorporate 3 deg (1-σ) initial state uncertainty and TC 3 and TC 4 include 10 deg (1-σ) initial state uncertainty in $\boldsymbol{\theta}_{\mathcal{I}}^{\mathcal{B}}$. When shape model bias is included (TC 2 and TC 4), an initial uncertainty of 0.5 mag (1-σ) is assumed. The baseline TC, TC1, and TC2 use 5,000 particles and TC 3 and TC 4 use 10,000 particles. In all test cases, there is a 'true' shape model (defined in Table 2(a)) and an 'estimated' shape model with associated parameter uncertainty (Tables 2(b) and 2(c), respectively). Both shape models define a cube with each side measuring 0.1m.

The measurement sequence, state estimation error, expected measurements, and measurement residuals of the baseline TC are given in Figures 3, 2(a), and 2(b), respectively. The true attitudes are θ_1 = 247.8 deg, θ_2 = 0 deg, and θ_3 = 133.1 deg. As intended, the PF performs well, reducing uncertainty in θ_2 and θ_3 and tracking the true attitude.

Table 1: Testcase Outline

Test Case	Dynamics	States	Maneuver	Est. Model	Note
Baseline	None	$\boldsymbol{\theta}_{\mathcal{I}}^{\mathcal{B}}$	None	True	Baseline
1	None	$\boldsymbol{\theta}_{\mathcal{I}}^{\mathcal{B}}$	None	Est.	Incorrect model divergence
2	Bias	$\boldsymbol{\theta}_{\mathcal{I}}^{\mathcal{B}}$, b_m	None	Est.	Uncertain shape model
3	Ang. Rate	$\boldsymbol{\theta}_{\mathcal{I}}^{\mathcal{B}}$	Slew	True	Agile SO
4	Ang. Rate & Bias	$\boldsymbol{\theta}_{\mathcal{I}}^{\mathcal{B}}$, b_m	Slew	Est.	Agile SO, uncertain shape model

Table 2: True and Estimated Unique Cube Shape Model Parameters

(a) True Shape Model Parameters

Face (in $\mathcal{B}$)	A (m)	ξ ( )	a ( )	m ( )
+Z	0.01	0.5	0.10	0.15
+Y	0.01	0.5	0.25	0.15
+X	0.01	0.5	0.40	0.15
-X	0.01	0.5	0.60	0.15
-Y	0.01	0.5	0.76	0.15
-Z	0.01	0.5	0.90	0.15

(b) Estimated Shape Model Parameters

Face (in $\mathcal{B}$)	A (m)	ξ ( )	a ( )	m ( )
+Z	0.01	0.4	0.25	0.25
+Y	0.01	0.4	0.30	0.25
+X	0.01	0.4	0.45	0.25
-X	0.01	0.4	0.65	0.35
-Y	0.01	0.4	0.80	0.35
-Z	0.01	0.4	0.95	0.35

(c) Estimated Shape Model Unc.

Face (in $\mathcal{B}$)	$\sigma_{\tilde{A}}$ ( )	$\sigma_{\tilde{\xi}}$ ( )	$\sigma_{\tilde{a}}$ ( )	$\sigma_{\tilde{m}}$ ( )
+Z	0.01	0.2	0.1	0.2
+Y	0.01	0.2	0.1	0.2
+X	0.01	0.2	0.1	0.2
-X	0.01	0.4	0.1	0.2
-Y	0.01	0.4	0.1	0.2
-Z	0.01	0.4	0.1	0.2

The measurement discrepancy is illustrated in Figure 3 where the lightcurves for both the true and estimated shape model, as well as the observed measurement sequence are plotted. As seen in Figure 3, the models differ as much as 1.3 apparent magnitudes (in excess of the 3-σ measurement uncertainty) for

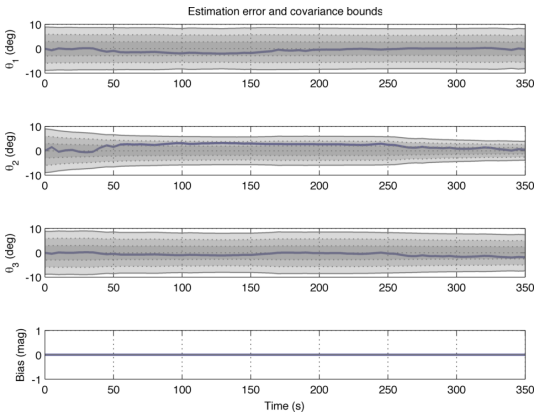

(a) Baseline state estimation error (estimate and 3-σ covariance bounds) for a nominal PF with no shape model error.

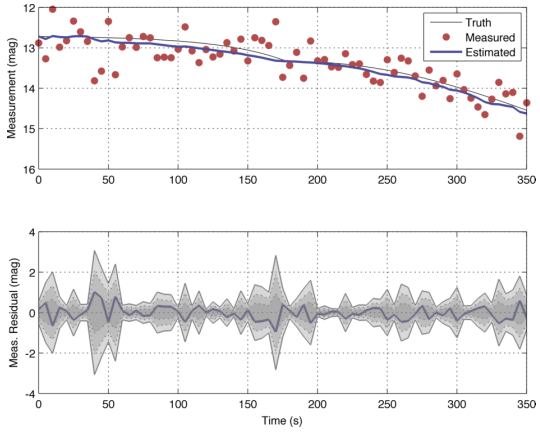

(b) Baseline post-update measurement estimate and residuals (with 3-σ bounds)

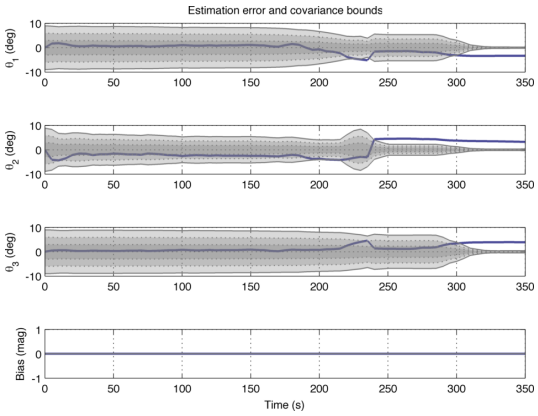

(c) TC 1 state estimation error (estimate and 3-σ covariance bounds). In this case filter divergence is expected because of shape model error.

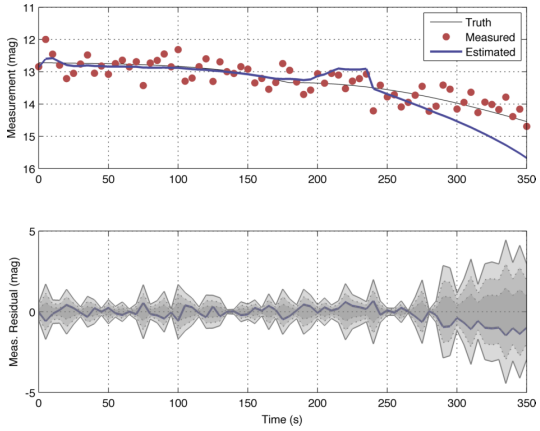

(d) TC 1 post-update measurement estimate and residuals (with 3-σ bounds)

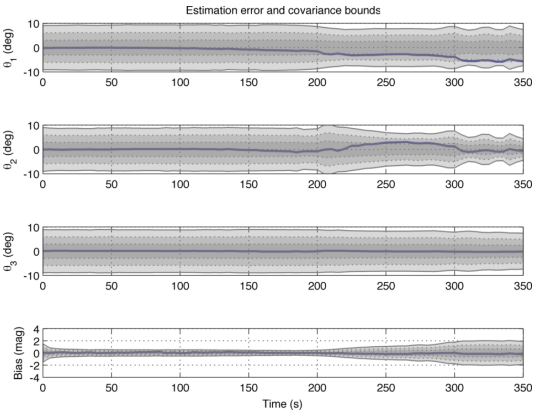

(e) TC 2 state estimation error (estimate and 3-σ covariance bounds)

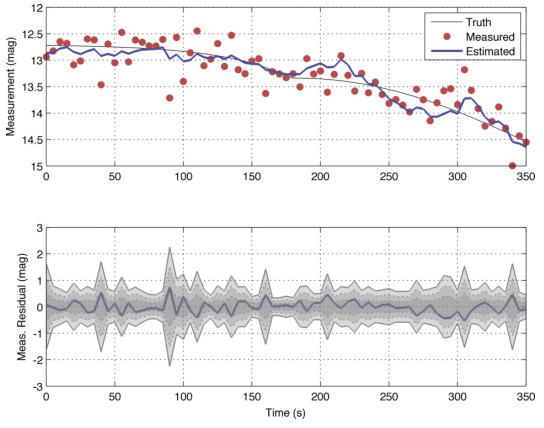

(f) TC 2 post-update measurement estimate and residuals (with 3-σ bounds)

Figure 2: Baseline TC, TC 1, and TC 2 results. N = 5000 particles

sustained periods of time. In 2(c) the state error diverges at t = 225s and the covariance of the PF reduces to unrealistically small values.

For TC 2, as shown in Figure 2(e), the PF estimate does not diverge and, despite modeling errors, is able to extract enough information from the measurement signal to improve the covariance bounds of the estimate. As shown in the bias covariance of Figure 2(e), just as the differences between the true and estimated shape models become large (see Figure 3), the computation of $Q_{\dot{b}_m}$ accounting for model uncertainty produces larger process noise inputs in the bias. This result supports directly supports a main contribution of this paper: incorporating shape model parameter uncertainty in the shape model bias dynamics can mitigate the deleterious effects of significant model uncertainty. TC 2 can also be directly compared to the baseline TC, where it is clear that the price for having an uncertain shape model is increased state uncertainty.

TC 3 endeavors to illustrate the utility of using the reduced order dynamics given in (3). In this scenario, the SO is maneuvering (as shown in Figure 4(a)) in excess of 20 deg for θ_1 and 50 deg for θ_3 over 350s. The initial true state is the same as in test cases 1 and 2. It is assumed for this test case (as well as test case 4) that $\mathbf{Q}_\omega = 1.0^2\mathbb{I}$ deg$^2/s^2$. The true and noisy apparent magnitude of the maneuvering SO are shown in Figure 4(b). For this particular test case, estimation error and error covariance are not plotted because the estimate becomes significantly non-Gaussian and multi-modal, reducing the utility of such measures. Rather, the PF particles at the final time (t = 350s) are shown in Figure 4(c). Note the multi-modal nature of the solution.

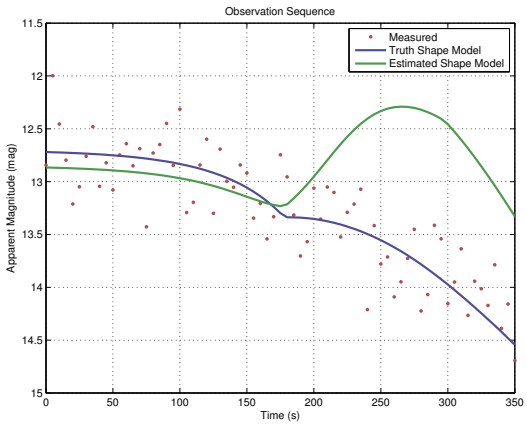

Figure 3: Baseline TC TC 1, and TC 2 measurement sequence. Blue is the true lightcurve and green is the lightcurve of the estimated model using the true attitude profile.

Immediately the non-Gaussian nature of the result in Figure 4(c)is apparent, as well as the fact that the PF with angular rate uncertainty dynamics was able to successfully track the true state. A much larger space of potential $\boldsymbol{\theta}_{\mathcal{I}}^{\mathcal{B}}$ values represent feasible estimated trajectories, in addition to the truth state. In practice, a careful balance between the assumed/possible angular rate uncertainty and desired accuracy must be chosen.

TC 4 incorporates both angular rate uncertainty and shape model estimate uncertainty in the dynamics (using (10)) for the maneuvering SO case found in test case 3. Because of the significant uncertainty in both the shape model and the angular rates, the regions of attitude space that the filter estimate encompasses are quite large. Critically the true state (the star in Figure 4(d)) is included in the distribution produced by the particle filter, so the combined approach is deemed successful.

4 SUMMARY

In this paper, lightcurve inversion approaches have been extended to agile, maneuvering SOs and cases with shape model error and uncertainty. Operational SO assumptions are used to eliminate dependence on mass properties and torque as inputs to the estimation process. A first-principles approach is used to derive first-order dynamics of the shape model bias in apparent magnitude due to relative SO motion and shape model uncertainty.

Several test cases are presented and discussed that demonstrate the utility of the individual and combined contributions of the approaches presented in this paper. First, the results show that incorporating shape model parameter uncertainty in the shape model bias dynamics can mitigate deleterious effects of significant shape model uncertainty. By linking model uncertainty through the dynamics, the particle filter automatically increases the state uncertainty, which keeps the state estimate from diverging due to the modeling error. When both satellite model error and slewing dynamics are introduced into the simulation, the non-Gaussian nature of the result state error distribution is apparent, highlighting why the use of the particle filter is advantageous. Even with the non-Gaussian error distribution, poor satellite model, and unknown attitude maneuver, the particle filter with angular rate uncertainty dynamics was able to successfully maintain the true state within the estimated error distribution.

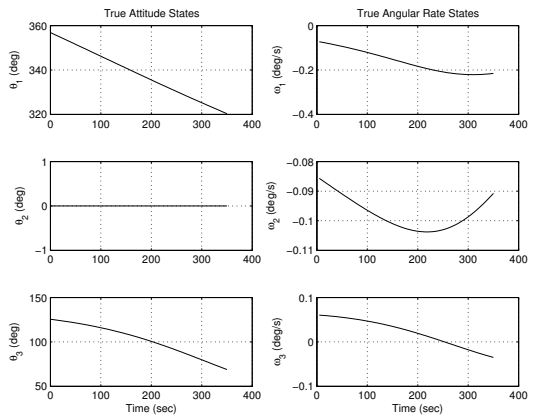

(a) Test case 3 & 4 true attitude and angular rate states

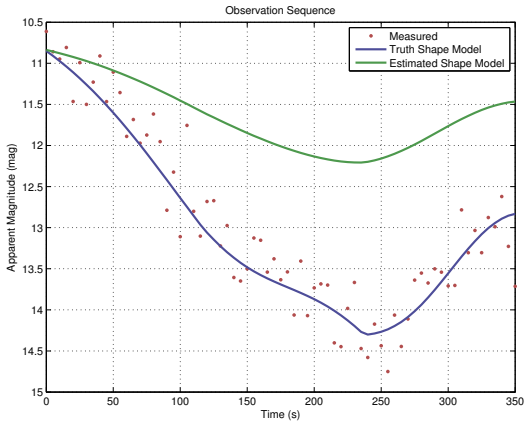

(b) Test case 3 & 4 Measurement sequence

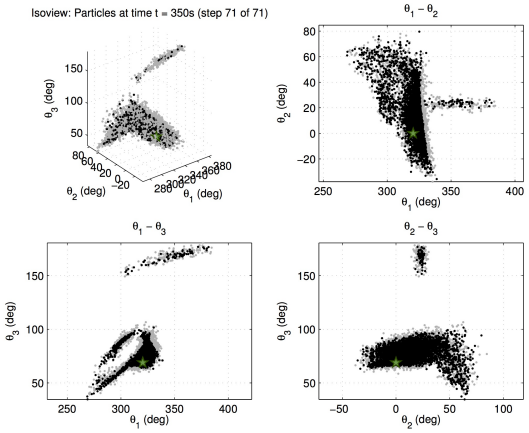

(c) Test case 3 Particle Filter at t_f = 350s. Grey dots are pre-measurement particles, black dots are post-measurement particles, and the star is the true state.

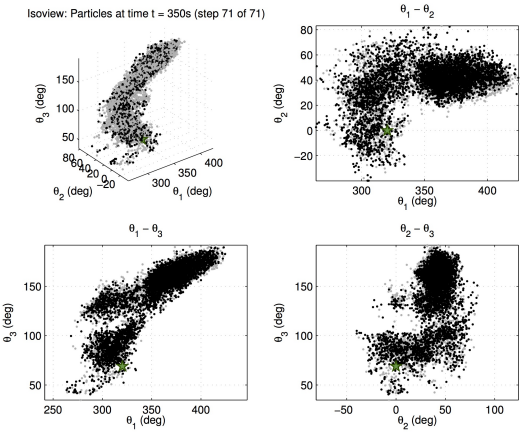

(d) Test case 4 Particle Filter at t_f = 350s. Grey dots are pre-measurement particles, black dots are post-measurement particles, and the star is the true state.

Figure 4: TC 3 and TC 4 results. N = 10000 particles

References

[1] L. James. On keeping the space environment safe for civil and commercial users, April 2009. Statement of Lieutenant General Larry James, Commander, Joint Functional Component Command for Space, Before the Subcommittee on Space and Aeronautics, House Committee on Science and Technology.

[2] Joint Chiefs of Staff. Space Operations. Joint Publication 3-14, January 2009.

[3] M. Kaasalainen, L. Lamberg, K. Lumme, and E. Bowell. Interpretation of lightcurves of atmosphereless bodies. I - General theory and new inversion schemes. *Astronomy and Astrophysics*, 259:318–332, June 1992.

[4] M. Kaasalainen, L. Lamberg, and K. Lumme. Interpretation of lightcurves of atmosphereless bodies. II - Practical aspects of inversion. *Astronomy and Astrophysics*, 259:333–340, June 1992.

[5] D. Hall, J. Africano, P. Kervin, and B. Birge. Non-imaging attitude and shape determination. In *Advanced Maui Optical and Space Surveillance Technologies Conference*, September 2005.

[6] D. Hall, B. Calef, K. Knox, M. Bolden, and P. Kervin. Separating attitude and shape effects for non-resolved objects. In *Advanced Maui Optical and Space Surveillance Technologies Conference*, September 2007.

[7] D. Hall, J. Africano, D. Archambealt, B. Birge, D. Witte, and P. Kervin. Amos observations of nasa's image satellite. In *Advanced Maui Optical and Space Surveillance Technologies Conference*, September 2006.

[8] R. L. Cook and K. E. Torrance. A reflectance model for computer graphics. *Computer Graphics*, 15(3):307–316, August 1981.

[9] C. J. Wetterer, S. Clayton, and J Stikeleather. Lightcurve inversion program for non-resolved space object identification. In *Maui High Performance Computing Center: Application Briefs 2006*, pages 8–9, 2006.

[10] M. Ashikhmin and P. Shirley. An anisotropic phong brdf model. *Journal of Graphical Tools*, 5(2):25–32, 2000.

[11] M. K. Jah and R. A. Madler. Satellite characterization: Angles and light curve data fusion for spacecraft state and parameter estimation. In *Advanced Maui Optical and Space Surveillance Technologies Conference*, September 2007.

[12] C. J. Wetterer and M. Jah. Attitude estimation from light curves. *Journal of Guidance, Control, and Dynamics*, 32(5):1648–1651, September-October 2009.

[13] R. Linares, J. L. Crassidis, M. K. Jah, and H. Kim. Astrometric and photometric data fusion for resident space object orbit, attitude, and shape determination via multiple-model adaptive estimation. In *AIAA Guidance, Navigation, and Control Conference*, August 2010. AIAA 2010-8341.

[14] B. Ristic, S. Arulampalam, and N. Gordon. *Beyond the Kalman Filter*, chapter 1, 3. Artech House, Boston, 2004.

[15] M. J. Holzinger, K. T. Alfriend, C. J. Wetterer, K. Luu, C. Sabol, K. Hamada, and A. Harms. Photometric attitude estimation for agile space objects with shape uncertainty. *Journal of Guidance, Control, and Dynamics*, In Press., 2013.

[16] H. Schaub and J. L. Junkins. *Analytical Mechanics of Space Systems, Second Edition*, chapter 3, 4. American Institute of Aeronautics and Astronautics, Inc., Reston, VA, 2009.

[17] P. Magnusson. Distribution of spin axes and senses of rotation for 20 large asteroids. *Icarus*, 68(1):1 – 39, 1986.

[18] M. Kaasalainen, J. Torppa, and J. Piironen. Models of twenty asteroids from photometric data. *Icarus*, 159(1):369–395, 2002.

[19] J. Torppa, M. Kaasalainen, T. Michalowski, T. Kwiatkowski, A. Kryszczynska, P. Denchey, and R. Kowalski. Shapes and rotational properties of thirty asteroids from photometric data. *Icarus*, 164(1):364–383, 2003.

[20] A. Ngan, F. Durand, and M. Wojciech. Experimental analysis of brdf models. In *Eurographics Symposium on Rendering*, April 2005.

[21] S. H. Westin, H. Li, and K. E. Torrance. A comparison of four brdf models. In *Eurographics Symposium on Rendering*, April 2004. PCG-04-2.

[22] D. T. Hall, J. L. Africano, J V. Lambert, and P. W. Kervin. Time-resolved i-band photometry of calibration spheres and nak droplets. *Journal of Spacecraft and Rockets*, 44(4):910–919, July 2007.

[23] N. J. Gordon, D. J. Salmond, and A. F. M. Smith. Novel approach to nonlinear/non-gaussian bayesian state estimation. *IEE Proc.-F*, 140(2):107–113, 1993.

[24] G. Kitagawa. Monte carlo filter and smoother for non-gaussian non-linear state space models. *Journal of Computational and Graphical Statistics*, 5(1):1–25, 1996.